

Laterally swept light-sheet microscopy enhanced by pixel reassignment for photon-efficient volumetric imaging

Liang Qiao,^{a,†} Hongjin Li^{✉, a,b,†} Suyi Zhong,^{c,†} Xinzhu Xu,^c Fei Su,^{a,d} Xi Peng,^{a,c} Dayong Jin,^{a,d,*} and Karl Zhanghao^{✉,a,*}

^aSouthern University of Science and Technology, College of Engineering, UTS-SUSTech Joint Research Centre for Biomedical Materials and Devices, Department of Biomedical Engineering, Shenzhen, China

^bCity University of Hong Kong, Department of Biomedical Engineering, Hong Kong, China

^cPeking University, College of Future Technology, Department of Biomedical Engineering, Beijing, China

^dUniversity of Technology Sydney, Institute for Biomedical Materials and Devices (IBMD), Faculty of Science, Sydney, Australia

Abstract. In light-sheet fluorescence microscopy, the axial resolution and field of view are mutually constrained. Axially swept light-sheet microscopy (ASLM) can decouple the trade-off, but the confocal detection scheme using a rolling shutter also rejects fluorescence signals from the specimen in the field of interest, which sacrifices the photon efficiency. Here, we report a laterally swept light-sheet microscopy (LSLM) scheme in which the focused beam is first scanned along the axial direction and subsequently laterally swept with the rolling shutter. We show that LSLM can obtain a higher photon efficiency when similar axial resolution and field of view can be achieved. Moreover, based on the principle of image scanning microscopy, applying the pixel reassignment to the LSLM images, hereby named iLSLM, improves the optical sectioning. Both simulation and experimental results demonstrate the higher photon efficiency with similar axial resolution and optical sectioning. Our proposed scheme is suitable for volumetric imaging of specimens that are susceptible to photobleaching or phototoxicity.

Keywords: light-sheet fluorescence microscopy; image scanning microscopy; volumetric imaging; pixel reassignment.

Received Aug. 9, 2022; revised manuscript received Oct. 11, 2022; accepted for publication Oct. 20, 2022; published online Dec. 5, 2022.

© The Authors. Published by SPIE and CLP under a Creative Commons Attribution 4.0 International License. Distribution or reproduction of this work in whole or in part requires full attribution of the original publication, including its DOI.

[DOI: [10.1117/1.APN.2.1.016001](https://doi.org/10.1117/1.APN.2.1.016001)]

1 Introduction

Light-sheet fluorescence microscopy has become an indispensable tool for biological imaging because of its high spatio-temporal resolution and low phototoxicity.^{1–3} It eliminates the out-of-focus excitation by illuminating the specimen from the side with a sheet of light.^{4,5} Therefore, most of the excited fluorophores can be collected by the detection camera. This excitation and detection scheme and the exclusion of pinholes significantly reduce photobleaching and phototoxicity, which makes it suitable for long-term imaging. In addition, the thin light sheet improves optical sectioning and provides better axial

resolution. However, generating a thin and uniform light sheet is difficult because the thickness and field of view (FoV) limit each other.⁶ For a typical Gaussian light sheet, the light sheet only covers a region of ~ 2 Rayleigh lengths, which is quadratically proportional to its thickness.

Propagation invariant beams can persist at a thin thickness over an arbitrarily long distance, including Bessel beams^{7–9} and Airy beams,^{10,11} while the conflict between light-sheet thickness and FoV remains. Moreover, these nondiffractive beams contain more sidelobes, which will introduce more out-of-focus illumination and increase phototoxicity.¹² Another method is to use multiple light sheets with swept focus¹³ or tiled beams.^{14–17} Swept focus light-sheet microscopy (SFLM) generates a virtual light sheet with a higher aspect ratio. However, multiple beams also introduce more sidelobes, which decrease the axial resolution and worsen the optical sectioning.

*Address all correspondence to Dayong Jin, dayong.jin@uts.edu.au; Karl Zhanghao, karl.hao.zhang@gmail.com

[†]These authors contributed equally to this work.

A slit can efficiently reject the sidelobes of the excitation beams. In light-sheet microscopy, the rolling shutter of sCMOS cameras can synchronize with the beam scanning and naturally serve as the slit. For example, the rolling shutter can eliminate the sidelobes of Gaussian beams¹⁸ or Bessel beams¹⁹ in digital scanned light-sheet microscopy. While the conflict between light-sheet thickness and FoV remains in these methods, axially swept light-sheet microscopy (ASLM) uses the synchronized rolling shutter of a camera to image only the in-focus region of a light sheet so that an arbitrarily large FoV with optimal axial resolution can be achieved.^{20,21} However, like the pinhole in confocal microscopes, the slit or the rolling shutter rejects many fluorescent signals and sacrifices the photon efficiency of light-sheet microscopy. As shown in Fig. 1(a), a Gaussian beam is first laterally scanned and subsequently axially swept in synchronization with the rolling shutter of the sCMOS camera. The fluorescence signal outside the rolling shutter is rejected, so a larger imaging FoV occurs at the price of less photon efficiency.

Imaging scanning microscopy (ISM) can achieve the optimal resolution of confocal microscopy without sacrificing the efficiency of photon collection.^{22,23} Array detectors are used in ISM to record images at each scan position. Each pixel of the array can act as a confocal pinhole to simultaneously acquire many

confocal images. Then, these confocal images are reassembled through pixel reassignment, either computer-based or optics-based.²⁴ The final image has the optimal resolution and optical sectioning of the confocal microscopy but with no light loss. We anticipate that the same principle can be applied to light-sheet microscopy with a swept focus. A series of images at different illumination foci can be acquired and reassembled with pixel reassignment. The final image should achieve improved axial optical sectioning with little loss of fluorescent signals. Thus, the tradeoff between light-sheet thickness and FoV can be decoupled without sacrificing the photon efficiency of fluorescent signals.

Here, we present the laterally swept light-sheet (LSLM) scheme, which is first scanned along the axial direction and subsequently laterally swept [Fig. 1(a)]. Compared with ASLM, this setup has two primary advantages. First, the excitation light is more constrained after axial scanning, so the majority of the excited fluorescence is within the rolling shutter and can be collected by the detection pixels. Second, the full width at half-maximum (FWHM) of the beam profile is much smaller than that of the ASLM, which makes it possible to adopt the ISM concept with pixel reassignment. In this paper, we systematically compare the ASLM and LSLM with simulation studies

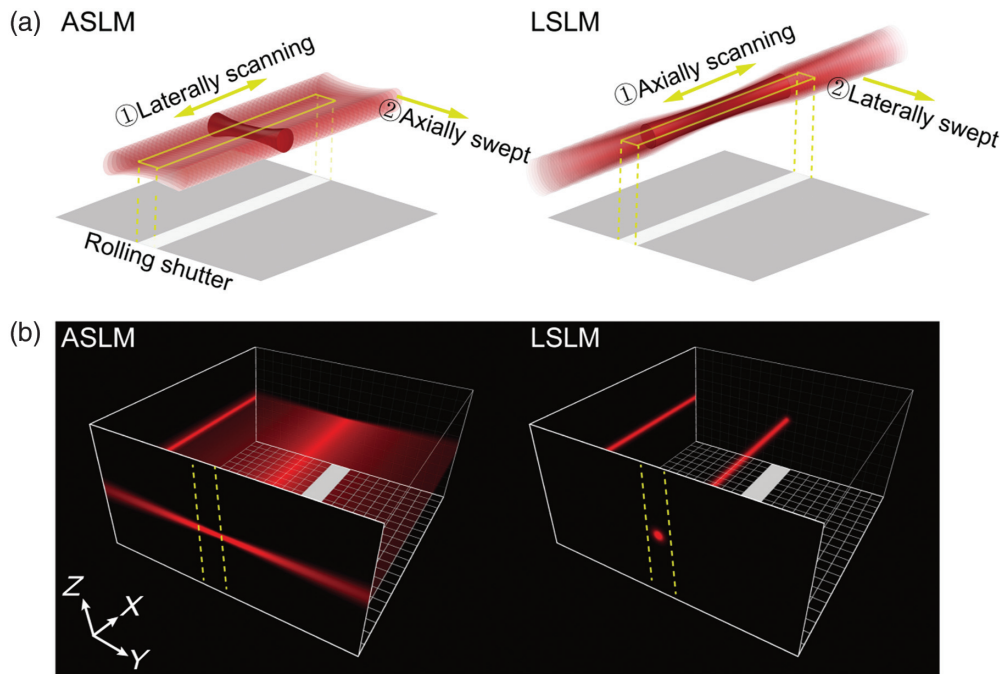


Fig. 1 Schematic comparison between the ASLM and LSLM. (a) In the ASLM, a focused Gaussian beam is first laterally scanned that generates a light sheet perpendicular to the direction of beam propagation. Afterward, the focus of the Gaussian beam is axially swept in synchronization with the rolling shutter of the camera. In the LSLM, a Gaussian beam is first axially scanned that forms a “light needle” along the direction of beam propagation. Then, the beam is laterally swept in synchronization with the camera. Here, the axial direction is along the propagation of the beam and the lateral direction is perpendicular to the propagation of the beam. With the rolling shutter, only the region excited by the in-focus, thin light sheet is imaged by the camera. (b) Comparison of light sheets generated by lateral scanning of the ASLM and axial scanning of the LSLM. The images on the Y–Z plane show the cross section of the light sheet, and the yellow dashed lines indicate the rolling shutter. With the same rolling shutter, the ASLM shows better axial optical sectioning, but the LSLM contains more excitation power in the shutter region, which is more photon-efficient.

and experiments to demonstrate that the LSLM shows better axial resolution than the ASLM when a high photon efficiency is required, particularly for the ISM-enhanced LSLM (iLSLM).

2 Principle of the LSLM

The scanning schematics of the ASLM and LSLM are compared in Fig. 1(a). In the ASLM, the lateral scanning of the Gaussian beams improves the axial resolution in the in-focus region. However, because the rolling shutter is applied perpendicular to the beam propagation direction, a large region of a specimen outside of the rolling shutter is excited, while the emitted fluorescence is not detected by the camera. When the fluorophores are widely distributed and excited by the light sheet, only the fluorescence within the rolling shutter can be detected, and the fluorescence outside the rolling shutter is wasted. A larger entire imaging FoV corresponds to a lower efficiency of fluorescence detection. When the rolling shutter becomes narrower, a higher axial resolution and better optical sectioning can be obtained at the cost of the lower collection efficiency of fluorescent signals. Therefore, the width of the rolling shutter is a balance between photon efficiency and axial resolution or optical sectioning.

In contrast, the Gaussian beams are first axially scanned in the LSLM, and the rolling shutter is applied along the beam propagation direction. Following the definition of the ASLM,^{20,21,25} we set the direction of the rolling shutter as the Y axis and term the beam propagation as the axial scanning direction. From the beam profiles along the Y axis [Fig. 1(b)], we find that the power of the LSLM light sheet is more constrained within the rolling shutter, which should be more photon-efficient. To quantitatively compare the performance between the ASLM and LSLM, we conduct theoretical simulations based on the scalar propagation model considering a coherent, monochromatic, and medium numerical aperture (N.A.) imaging system. The simulation was performed based on the beam simulator software developed by Remacha et al.⁶ Briefly, the beam intensity distribution is

$$I = |E(x, z; y)|^2, \quad (1)$$

where

$$E(x, z; y) = \mathcal{F}[E(k_x, k_z) \exp(ik_y \Delta y)], \quad (2)$$

where $E(x, z; y)$ is the electricity distribution. $E(k_x, k_z)$ is the electricity distribution in the back focus plane (BFP). y is the position along the propagation direction with Δy from the focus. $k_y = \sqrt{(nk_0)^2 - (k_x^2 + k_z^2)}$, where n is the refraction index, and $k_0 = 2\pi/\lambda$ is the vacuum wavenumber. For a Gaussian beam, the amplitude at the BFP can be considered as

$$E(k_x, k_z) = \exp[-(k_x^2 + k_z^2)/(k_0 \text{N.A.})^2], \quad (3)$$

where N.A. is the numerical aperture of the excitation objective.

In Fig. 2, we set N.A. = 0.3, $n = 1.33$, $\lambda = 473$ nm, and the imaging FoV is $300 \mu\text{m} \times 300 \mu\text{m}$ in the simulation, which is consistent with our experimental settings. The simulation with N.A. = 0.5 (Fig. S1 in the [Supplementary Material](#)) yields similar results. The focused Gaussian beam simulated with Eqs. (1)–(3) is first laterally or axially scanned [Figs. 2(a) and 2(b)], and the scanned beams that fall within the depth

of focus of the detected objective ($\sim 14.4 \mu\text{m}$ for detection N.A. = 0.3) are summed to generate the scanned light sheet. In swept focus light-sheet microscopy, the focused Gaussian beam is both laterally and axially scanned [Fig. 2(c)]. The Z axis profiles at the focus in Fig. 2(d) show the axial resolution and optical sectioning of the light sheets in the ASLM, LSLM, and SFLM. The ASLM ($\text{FWHM}_{\text{ASLM}} = 0.81 \mu\text{m}$) and LSLM ($\text{FWHM}_{\text{LSLM}} = 0.88 \mu\text{m}$) show approximately tripled axial resolution of the SFLM ($\text{FWHM}_{\text{SFLM}} = 2.41 \mu\text{m}$).

Although the axial FWHM of the LSLM is close to that of the ASLM, the axial scanning in the LSLM will introduce larger sidelobes in the “light needle” [Fig. 2(d)], and the problem of sidelobes will become more severe when the scanning FoV increases. The optical sectioning width (OS), which is defined as the range containing 63% (obtained by $1 - 1/e$) of the detected beam power,¹² is $\text{OS}_{\text{ASLM}} = 0.69 \mu\text{m}$, $\text{OS}_{\text{LSLM}} = 2.32 \mu\text{m}$, and $\text{OS}_{\text{SFLM}} = 8.46 \mu\text{m}$, respectively. In contrast, the light-sheet thickness of laterally scanned beams in the ASLM is diffraction-limited. In summary, both the LSLM and ASLM show approximately tripled axial resolution of the conventional SFLM, and both have thinner optical sectioning. While the LSLM still has a similar axial resolution to the ASLM, the LSLM has worse optical sectioning than the ASLM. However, the FWHM of the axial scanning beams is close to the diffraction limit on both the Y axis and Z axis, so the pixel reassignment can effectively eliminate the sidelobe effect of the LSLM.

3 Pixel Reassignment Increases the Optical Sectioning of the LSLM

The photon efficiency is related to the energy ratio of the detected fluorescence within the rolling shutter to all the emitted fluorescence throughout the FoV. The relationship between the energy ratio and the width of the rolling shutter is plotted in Fig. 2(f). In addition, the relationships between the axial FWHM and the rolling shutter width are plotted in Fig. 2(g). A larger rolling shutter will result in a higher photon efficiency but worse axial resolution and optical sectioning. To fairly compare the ASLM and LSLM, we plot their axial resolutions corresponding to the same energy ratio in Fig. 2(h). When a high energy ratio or photon efficiency is required, LSLM shows about 9% improvement in the axial resolution compared to the ASLM in terms of the axial FWHM. For example, the highlighted regions in Figs. 2(a) and 2(b) indicate the appropriate shutter widths of $86.0 \mu\text{m}$ for the ASLM and $3.6 \mu\text{m}$ for the LSLM, within which they both have an energy ratio of $\sim 50\%$ and an axial FWHM of $\sim 1.2 \mu\text{m}$. When an energy ratio above 18% (10%, N.A. = 0.5) is desired, the LSLM creates a thinner axial FWHM than the ASLM.

Nevertheless, the optical sectioning of the LSLM is about three times thicker than that of the ASLM, so we will try to eliminate the sidelobe effect in the LSLM with pixel reassignment. Since the LSLM has a comparable resolution along the scanning axis to the detection point spread function (PSF), pixel reassignment based on the ISM principle can increase the axial resolution and improve optical sectioning. In this work, we only apply the digital pixel reassignment to the multiple raw images, so that the imaging results of the ASLM, LSLM, and iLSLM are processed from the same raw data to guarantee a fair comparison. The drawback is that the digital pixel reassignment requires more raw images and takes a longer acquisition time.

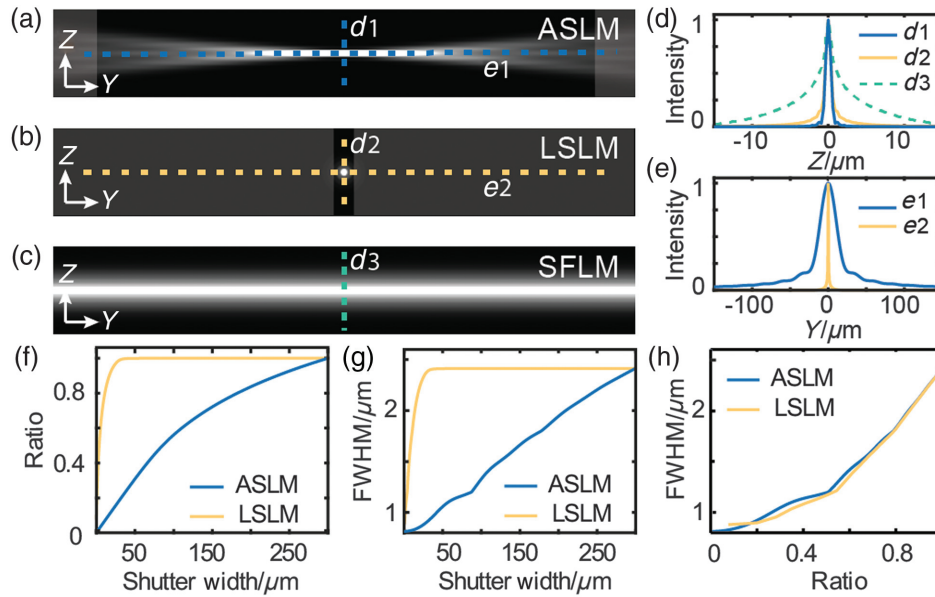


Fig. 2 Comparison between the ASLM and LSLM with simulation studies. Cross-sectional view of the light sheet with a cropped Y-FoV of $100\ \mu\text{m}$ in the Y–Z plane after the first scanning for (a) the ASLM and (b) the LSLM. The highlighted region shows an example of the rolling shutter with a width of $\sim 86.0\ \mu\text{m}$ for the ASLM and $\sim 3.6\ \mu\text{m}$ for the LSLM, for which the energy ratios are both $\sim 50\%$ and the axial FWHM are both $\sim 1.2\ \mu\text{m}$ for the two models. Scale bar: $10\ \mu\text{m}$. (c) Cross-sectional view of the SFLM in the Y–Z plane generated by lateral and axial scanning without confocal detection. (d) Intensity profiles along the Z axis for d_1 , d_2 , and d_3 . The FWHM is $0.81\ \mu\text{m}$ for the ASLM, $0.88\ \mu\text{m}$ for the LSLM, and $2.41\ \mu\text{m}$ for the SFLM. (e) Intensity profiles along the Y axis for e_1 and e_2 . (f) The energy ratio changes with rolling shutter widths for both the ASLM and LSLM. (g) The axial FWHM increases with a larger rolling shutter width for both the ASLM and LSLM. (h) Relationship between the axial FWHM and energy ratio.

In our experiments, 22 axial scanning and 30 lateral scanning are performed, acquiring 660 raw images for one scanning cycle. Nevertheless, the acquisition of the raw images at every focus is for a fair comparison of the ASLM, LSLM, and iLSLM. In real experiments, the axial scanning of the iLSLM can be performed within one exposure since the refreshing rate of the spatial light modulator (SLM) is fast enough. Therefore, only 30 images with lateral scanning are acquired for reconstruction with pixel reassignment, resulting in a 30-fold increase of the acquisition time. Optical ISM²⁴ can also achieve doubled spatial resolution. In the all-optical realization, the pixel reassignment is achieved by the descanning or rescanning of the emitted fluorescence. The drawback is that the scaling of the focused image is determined by the two-lens relay optics and is fixed. However, optical pixel reassignment can obtain the super-resolution image in one frame, which is in principle applicable and remains to be our future work.

The spatial resolution of ISM can be quantitatively described as²³

$$\sigma_{\text{ISM}} = (1/\sigma_{\text{exc}}^2 + 1/\sigma_{\text{det}}^2)^{-1/2}, \quad (4)$$

when the detected photon is reassigned to the excitation center by a factor of $m = \sigma_{\text{exc}}^2 / (\sigma_{\text{exc}}^2 + \sigma_{\text{det}}^2)$.²⁴ The excitation PSF, detection PSF, and PSF of the ISM are approximated by Gaussian functions, and σ_{exc} , σ_{det} , and σ_{ISM} are the corresponding

standard deviations. To obtain a higher resolution in ISM (smaller σ_{ISM}), σ_{exc} and σ_{det} should be as small as possible. While σ_{det} is determined by the detection objective and fixed, σ_{exc} is determined by the beam type of the light sheet. For the ASLM, σ_{exc} relates to the axial profile of the Gaussian PSF, which is much larger than that of the lateral profile. Therefore, the combination of the ISM and ASLM will slightly enhance the spatial resolution and optical sectioning due to the difference between σ_{exc} and σ_{det} . In comparison, the σ_{exc} and σ_{det} are close in the LSLM, which can better increase the spatial resolution.

To verify the performance of pixel reassignment in the LSLM, we simulate the ASLM and LSLM imaging of fluorescent beads in a 3D volume. We set N.A. = 0.3, $n = 1.33$ for both excitation and detection, $\lambda = 473\ \text{nm}$ and $525\ \text{nm}$ for excitation and detection, respectively, voxel size of $720\ \text{nm}$, and imaging volume of $72\ \mu\text{m} \times 720\ \mu\text{m} \times 72\ \mu\text{m}$, which is consistent with our experimental settings. The bead size in the simulation is set to be one voxel. The first step of the simulation is the same for the ASLM and LSLM. A focused Gaussian beam is axially and laterally scanned to excite the specimen. A series of images are simulated in which each image is excited by a single-focus Gaussian light sheet. Therefore, the ASLM and LSLM results are generated from the same dataset and compared under identical conditions. Next, we simulate the lateral scanning of the ASLM by summing the laterally scanned images and simulate the axially scanned “light needle” of the LSLM by summing the axially scanned images, as illustrated in Fig. 1.

The imaging process of the first step could be expressed as

$$I_{\text{ASLM1}}(x, y - y_s; z - z_s) = \left[o(x, y; z - z_s) \sum_{x_s} I_{\text{ex}}(x - x_s, z; y - y_s) \right] * h_{\text{det}}(x, y; z), \quad (5)$$

$$I_{\text{LSLM1}}(x - x_s, y; z - z_s) = \left[o(x, y; z - z_s) \sum_{y_s} I_{\text{ex}}(x - x_s, z; y - y_s) \right] * h_{\text{det}}(x, y; z), \quad (6)$$

where $I_{\text{ASLM1}}(x, y - y_s; z - z_s)$ and $I_{\text{LSLM1}}(x - x_s, y; z - z_s)$ are the signals delivered by the imaging system after first scanning for the ASLM and LSLM, respectively. $o(x, z; y)$ is the bead distribution, $I_{\text{ex}}(x - x_s, z; y - y_s)$ is the focused Gaussian beam for excitation at the lateral and axial scanning positions x_s and y_s , $*$ means convolution and $h_{\text{det}}(x, y; z)$ is the detection PSF. Only the in-focus signal is captured by the camera, and a digital slit mask that serves as the rolling shutter is applied to each image during the second scanning

$$I_{\text{ASLM2}}(x, y - y_s; z_0 - z_s) = I_{\text{ASLM1}}(x, y - y_s; z_0 - z_s) S(x, y - y_s), \quad (7)$$

$$I_{\text{LSLM2}}(x - x_s, y; z_0 - z_s) = I_{\text{LSLM1}}(x - x_s, y; z_0 - z_s) S(x - x_s, y), \quad (8)$$

where $I_{\text{ASLM2}}(x, y - y_s; z_0 - z_s)$ and $I_{\text{LSLM2}}(x - x_s, y; z_0 - z_s)$ are the recorded signals in the second scanning for the ASLM and LSLM, respectively. $I_{\text{ASLM1}}(x, y; z_0 - z_s)$ and $I_{\text{LSLM1}}(x, y; z_0 - z_s)$ are the signals on the detection focal plane after first scanning for the ASLM and LSLM. $S(x, y - y_s)$ and $S(x - x_s, y)$ are the rolling shutters on the conjunction positions of excitations for the ASLM and LSLM, respectively. Finally, a 3D stack of images could be obtained considering all the scanning positions

$$I_{\text{ASLM}}(x, y; z_s) = \sum_{y_s} I_{\text{ASLM2}}(x, y - y_s; z_0 - z_s), \quad (9)$$

$$I_{\text{LSLM}}(x, y; z_s) = \sum_{x_s} I_{\text{LSLM2}}(x - x_s, y; z_0 - z_s), \quad (10)$$

in which $I_{\text{ASLM}}(x, y; z_s)$ and $I_{\text{LSLM}}(x, y; z_s)$ are the final ALSM and LSLM images, respectively.

For iLSLM, pixel reassignment is applied to LSLM images during the second scanning. The image is scaled down by a factor of $m = \sigma_{\text{exc}}^2 / (\sigma_{\text{exc}}^2 + \sigma_{\text{det}}^2)$, which in practice is set to be $1/2$ as σ_{exc} and σ_{det} are close in the LSLM, along the swept direction at each focus position. For the fluorophores with a large Stokes shift or with multiphoton excitation, the σ_{exc} and σ_{det} will be different because of the different excitation wavelengths and emission wavelengths, so the scaling factor should be chosen based on the equation. Then, the images are placed back in the same position and summed to obtain the final iLSLM image

$$I_{\text{iLSLM}}(x, y; z_s) = \sum_{x_s} I_{\text{LSLM2}}\left(\frac{x - x_s}{m}, y; z_0 - z_s\right). \quad (11)$$

When all images are summed without a digital rolling shutter applied, the resulting image is equivalent to the SFLM image. The SFLM image collects more fluorescence signals but contains heavier sidelobes. Therefore, the photon efficiency of the ASLM and LSLM is calculated based on the SFLM image. Figures 3(a) and 3(b) show the simulated imaging results of fluorescence beads in the X - Y and X - Z planes. The upper part of Fig. 3(c) shows the profiles of the ASLM and iLSLM at 55% photon efficiency, and they have an axial FWHM of about $1.09 \mu\text{m}$. The lower part of Fig. 3(c) shows the profiles of the ASLM and iLSLM at 80% photon efficiency, and the iLSLM has a higher axial resolution ($\text{FWHM}_{\text{iLSLM}} = 1.15 \mu\text{m}$) than the ASLM ($\text{FWHM}_{\text{ASLM}} = 1.58 \mu\text{m}$). We calculated the changes in the photon efficiency of the ASLM and iLSLM with increasing rolling shutter over the entire ratio range, and the results are shown in Fig. 3(d). As shown in Fig. 3(f), the iLSLM has a smaller axial FWHM than the ASLM at the same photon efficiency when the photon efficiency is higher than 55%. The “turning point” of 55% is related to the N.A. of the objective, but is not affected by the signal-to-noise ratio (SNR), according to further simulation studies in Fig. S2 in the [Supplementary Material](#). Therefore, when the specimen is easy to photobleach or susceptible to phototoxicity, the iLSLM is a better choice than the ASLM.

4 Microscope Setup and Experimental Demonstration

We build a light-sheet microscope as shown in Fig. 4(a) that modulates the beam focus via a reflectively binary phase SLM. The SLM modulates the phase of the exciting light wave front and scans the beam in three dimensions. The pattern loaded for the SLM is calculated as described in previous work.^{14,16} Briefly, we take the SLM as a thin focusable lens for axial scanning whose phase modulation function to achieve axial defocus Δy can be expressed as

$$\phi_{\text{axial}}(x, z) = -k\Delta y(x_m^2 + z_n^2)/2f_{\text{scan}}^2, \quad (12)$$

where x_m and z_n are the central coordinates of row m and column n of the SLM space pixel, respectively, k is the wavenumber of the incident beam, Δy is the axial focus shift, and f_{scan} is the focal length of scan lens L2.

For lateral scanning, the SLM can be considered as a grating. Therefore, we applied the beam tilt phase delay in the SLM. The function can be expressed as

$$\phi_{\text{lateral}}(x, z) = k(x_m \sin \theta_x + z_n \sin \theta_z), \quad (13)$$

where θ_x and θ_z are the deflection angles of the beam in the x and z directions, respectively. We obtain the lateral coordinates (x_s, z_s) from the geometric relationship with the scanning deflection angle (θ_x, θ_z) , denoted as

$$\Delta x = f_{\text{scan}} \tan \theta_x, \quad \Delta z = f_{\text{scan}} \tan \theta_z. \quad (14)$$

When the SLM is loaded with patterns without additional phase information, the beam is focused at the focus of the scan lens, as shown in Fig. 4(b). By loading the SLM with different patterns

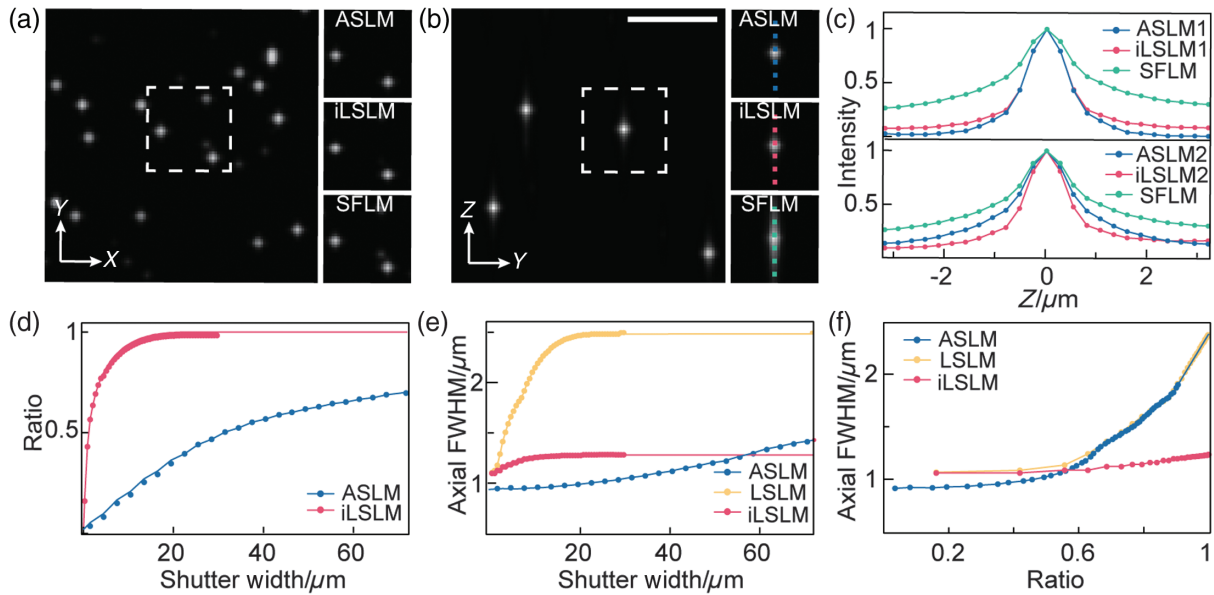


Fig. 3 Simulated imaging results of fluorescent beads. (a) and (b) Simulated imaging results of fluorescence beads in the X - Y and X - Z planes, and the three insets show the imaging results of the white dashed areas in the ASLM, iLSLM, and SFLM. (c) The upper and lower parts show the profiles of the ASLM, iLSLM, and SFLM when the photon efficiencies reach 58% and 80%, respectively. (d) and (e) Simulations to compare the photon efficiency and the axial FWHM of the ASLM and iLSLM with increasing rolling shutter. (f) Relationship between photon efficiency and the axial FWHM of the ASLM and iLSLM. Scale bar: $10\ \mu\text{m}$.

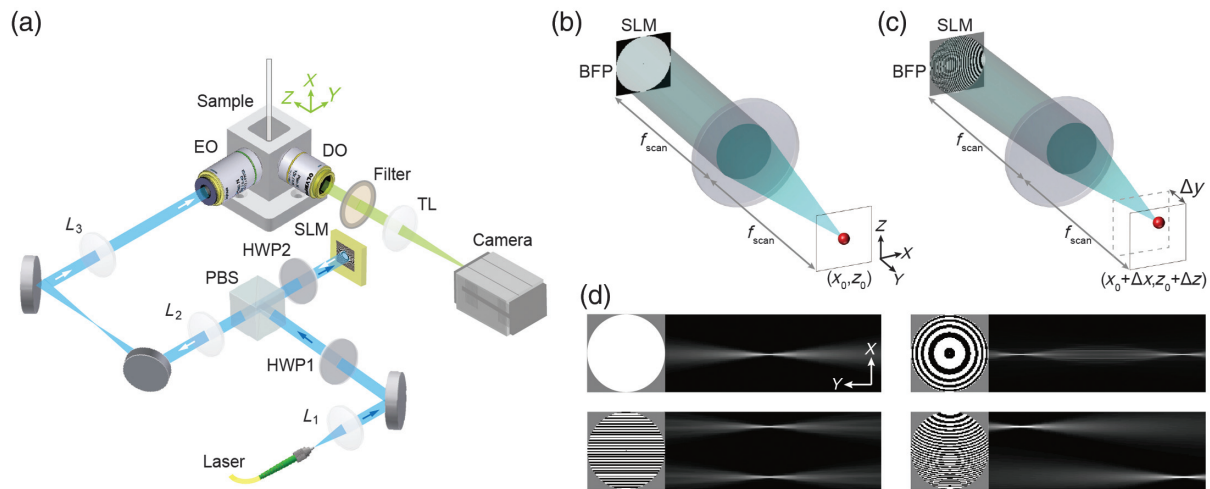


Fig. 4 The microscopy setup and focus scanning with the SLM. (a) Schematic diagram of the light sheet microscope. Laser: 473 nm, bandwidth 0.2 nm, MBL-III-473, CNI; $L_1 - L_3$: achromatic plano-convex lens, $L_1 = 50\ \text{mm}$, $L_2 = 250\ \text{mm}$, $L_3 = 250\ \text{mm}$; HWP1 and HWP2: half-wavelength plate, WPA2420-450-650, Union Optic; PBS, polarization beam splitter; CCM1-PBS251/M, Thorlabs; SLM, spatial light modulator, QXGA-R11, ForthDD; EO: excitation objective Lens, 20X/N.A. W, Olympus; DO: detection objective Lens, 10X/N.A. W, Olympus; Filter: ET525/50 M, Chroma; TL: tube lens, 200 mm, C60-TUBE B, ASI; Camera: ORCA-Flash 4.0, Hamamatsu. (b) and (c) When a binary phase pattern is loaded onto the SLM, the focus of the beam can be scanned in three dimensions. (d) Corresponding images when different phase patterns are loaded onto the SLM.

with additional phase information, we achieve 3D focus scanning, as shown in Figs. 4(c) and 4(d).

The LSLM and ASLM results are generated from the same dataset that consists of single-focus images. Then, we process

the raw images following Eqs. (4)–(11) to obtain the LSLM, ASLM, and SFLM results. Figures 5(a) and 5(b) show the experimental imaging of 200 nm fluorescence beads (F8888, Thermofisher) in the X - Y and X - Z planes, when the photon

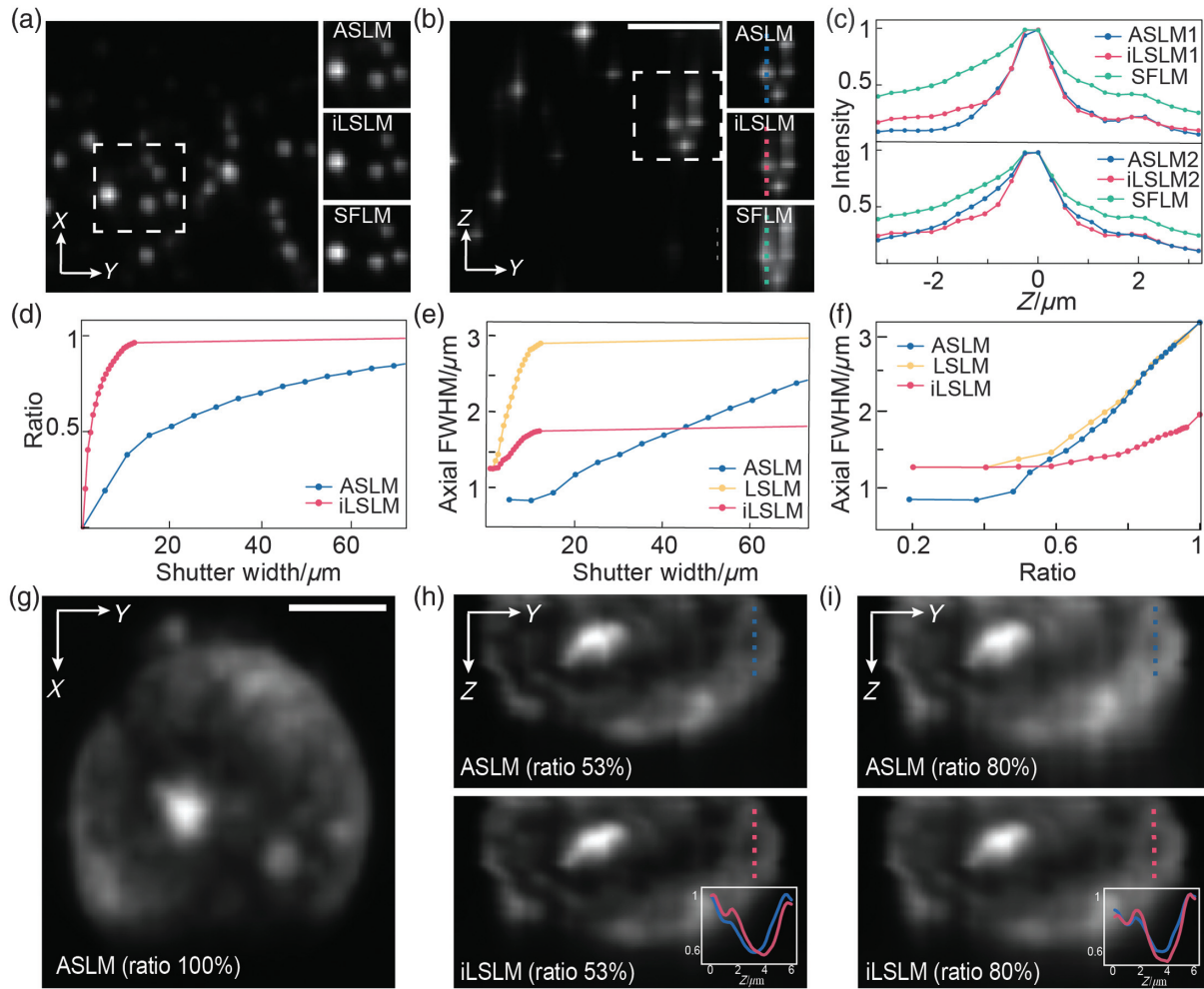


Fig. 5 Experimental imaging results of fluorescent beads and U2OS cells. (a) and (b) Experimental imaging results of fluorescence beads in the X - Y and X - Z planes, and the three insets show the imaging results of the white dashed areas in the ASLM, iLSLM, and SFLM. (c) The upper and lower parts show the profiles of the ASLM, iLSLM, and SFLM when the photon efficiencies reach 58% and 80%, respectively. (d) and (e) The photon efficiency and axial FWHM of the ASLM and iLSLM corresponding to the increasing rolling shutter. (f) Relationship between the photon efficiency and the axial FWHM of the ASLM and the iLSLM. (g)–(i) The ASLM and iLSLM imaging results of U2OS cells corresponding to the photon efficiencies of 53% and 80%. Scale bar: 10 μm .

efficiencies of the ASLM and iLSLM are at 58%. In Fig. 5(a), the lateral resolution of the iLSLM can reach 1.43 μm . The upper part of Fig. 5(c) shows the profiles of the iLSLM ($\text{FWHM}_{\text{iLSLM}} = 1.28 \mu\text{m}$, $\text{OS}_{\text{iLSLM}} = 2.69 \mu\text{m}$) and ASLM ($\text{FWHM}_{\text{ASLM}} = 1.35 \mu\text{m}$, $\text{OS}_{\text{ASLM}} = 2.04 \mu\text{m}$) at a photon efficiency of 58%. The lower part shows the profiles of the iLSLM ($\text{FWHM}_{\text{iLSLM}} = 1.60 \mu\text{m}$, $\text{OS}_{\text{iLSLM}} = 2.99 \mu\text{m}$) and ASLM ($\text{FWHM}_{\text{ASLM}} = 2.19 \mu\text{m}$, $\text{OS}_{\text{ASLM}} = 2.91 \mu\text{m}$) when the photon efficiency reaches 80%. The experimental results are consistent with the simulation results, which demonstrates that the ISM method can effectively improve the axial resolution and optical sectioning of the LSLM. Similarly, we analyze the relationship among the rolling shutter width, axial resolution, and photon efficiency in Figs. 5(d)–5(f). We further imaged the U2OS cells with the proposed scheme. Figure 5(g) shows the X - Y view of the U2OS cell, and Figs. 5(h)–5(i) compare

the X - Z images of the ASLM and iLSLM under the same photon efficiencies of 53% and 80%. By analyzing the simulation results and experimental results, we can conclude that the iLSLM has a better axial FWHM and optical sectioning than the ASLM when the photon efficiency exceeds 55%.

5 Conclusions

We propose the iLSLM scheme, which is laterally swept light-sheet microscopy with pixel reassignment based on the principle of an image scanning scope. First, we illustrate the generation of an axially swept light sheet and a laterally swept light sheet and compare their beam profiles. The laterally swept light sheet is more constrained and avoids the excitation of the specimen outside the rolling shutter. When all the final results are processed from the same raw data, both the LSLM and ASLM are three

times better than the conventional SFLM in axial resolution and optical sectioning. The LSLM has a similar axial resolution to the ASLM, while the optical sectioning of the LSLM is worse. However, the iLSLM with pixel reassignment outperforms the ASLM in either axial resolution or optical sectioning when >55% photon efficiency is required. Here, the calculation of the photon efficiency assumes linear photobleaching or phototoxicity. Because the scanning process results in a duty cycle of excitation, the peak excitations of the ASLM and LSLM are larger than that of a digital scanned light sheet using a Bessel beam or the ASLM using a cylindrical lens, which is investigated in Fig. S3 in the [Supplementary Material](#). Therefore, non-linear photobleaching should be avoided during the experiments when using the ASLM or LSLM. In this paper, no deconvolution was applied to the SFLM, ASLM, LSLM, or iLSLM. Further deconvolution¹³ or Fourier filtering can further increase the resolution and contrast of images.

In the current work, pixel reassignment is performed by digital image processing, which guarantees a fair comparison among the SFLM, ASLM, LSLM, and iLSLM. However, digital pixel reassignment requires multiple raw images and reduces the imaging speed. Optical pixel reassignment²⁴ can be implemented with the iLSLM in the future, which can achieve the super-resolution image within one exposure. Unlike the conventional ISM that scans the beam focus in two dimensions, the iLSLM setup only scans the beam along the *X* axis, which is easier to implement. With the improvement, the iLSLM can potentially be used in many applications where photobleaching is a severe problem or the specimen is susceptible to phototoxicity.

Acknowledgments

This work was supported by the National Natural Science Foundation of China (62005116 and 51720105015) and the Science and Technology Innovation Commission of Shenzhen (KQTD20170810110913065 and 20200925174735005). The authors declare no competing financial interests.

Data Availability Statement

The data that support the findings of this study are available from the corresponding author upon reasonable request.

References

1. E. H. K. Stelzer et al., "Light sheet fluorescence microscopy," *Nat. Rev. Methods Primers* **1**, 73 (2021).
2. O. E. Olarte et al., "Light-sheet microscopy: a tutorial," *Adv. Opt. Photonics* **10**, 111–179 (2018).
3. R. M. Power and J. Huisken, "A guide to light-sheet fluorescence microscopy for multiscale imaging," *Nat. Methods* **14**, 360–373 (2017).
4. A. H. Voie, D. H. Burns, and F. A. Spelman, "Orthogonal-plane fluorescence optical sectioning: three-dimensional imaging of macroscopic biological specimens," *J. Microsc.* **170**, 229–236 (1993).
5. J. Huisken et al., "Optical sectioning deep inside live embryos by selective plane illumination microscopy," *Science* **305**, 1007–1009 (2004).
6. E. Remacha et al., "How to define and optimize axial resolution in light-sheet microscopy: a simulation-based approach," *Biomed. Opt. Express* **11**, 8–26 (2020).
7. L. Gao et al., "3D live fluorescence imaging of cellular dynamics using Bessel beam plane illumination microscopy," *Nat. Protocol* **9**, 1083–1101 (2014).
8. T. A. Planchon et al., "Rapid three-dimensional isotropic imaging of living cells using Bessel beam plane illumination," *Nat. Methods* **8**, 417–423 (2011).
9. B. C. Chen et al., "Lattice light-sheet microscopy: imaging molecules to embryos at high spatiotemporal resolution," *Science* **346**, 1257998 (2014).
10. N. A. Hosny et al., "Planar Airy beam light-sheet for two-photon microscopy," *Biomed. Opt. Express* **11**, 3927–3935 (2020).
11. T. Vetterburg et al., "Light-sheet microscopy using an Airy beam," *Nat. Methods* **11**, 541–544 (2014).
12. B. J. Chang, K. M. Dean, and R. Fiolka, "Systematic and quantitative comparison of lattice and Gaussian light-sheets," *Opt. Express* **28**, 27052–27077 (2020).
13. K. M. Dean and R. Fiolka, "Uniform and scalable light-sheets generated by extended focusing," *Opt. Express* **22**, 26141–26152 (2014).
14. L. Gao, "Extend the field of view of selective plan illumination microscopy by tiling the excitation light sheet," *Opt. Express* **23**, 6102–6111 (2015).
15. L. Gao et al., "Lattice light sheet microscopy using tiling lattice light sheets," *Opt. Express* **27**, 1497–1506 (2019).
16. C. Liu et al., "Extended field of view of light-sheet fluorescence microscopy by scanning multiple focus-shifted Gaussian beam arrays," *Opt. Express* **29**, 6158–6168 (2021).
17. H. Li et al., "Axially overlapped multi-focus light sheet with enlarged field of view," *Appl. Phys. Lett.* **118**, 223701 (2021).
18. E. Baumgart and U. Kubitschek, "Scanned light sheet microscopy with confocal slit detection," *Opt. Express* **20**, 21805–21814 (2012).
19. F. O. Fahrbach and A. Rohrbach, "Propagation stability of self-reconstructing Bessel beams enables contrast-enhanced imaging in thick media," *Nat. Commun.* **3**, 632 (2012).
20. T. Chakraborty et al., "Light-sheet microscopy of cleared tissues with isotropic, subcellular resolution," *Nat. Methods* **16**, 1109–1113 (2019).
21. F. F. Voigt et al., "The mesoSPIM initiative: open-source light-sheet microscopes for imaging cleared tissue," *Nat. Methods* **16**, 1105–1108 (2019).
22. C. J. R. Sheppard, "Super-resolution in confocal imaging," *Optik* **80**, 53–54 (1988).
23. C. B. Muller and J. Enderlein, "Image scanning microscopy," *Phys. Rev. Lett.* **104**, 198101 (2010).
24. I. Gregor and J. Enderlein, "Image scanning microscopy," *Curr. Opin. Chem. Biol.* **51**, 74–83 (2019).
25. K. M. Dean et al., "Deconvolution-free subcellular imaging with axially swept light sheet microscopy," *Biophys. J.* **108**, 2807–2815 (2015).

Liang Qiao received his BS and MS degrees from Xi'an University of Technology in 2018 and 2021, respectively. He is currently working at Southern University of Science and Technology, Shenzhen, China. His research interests include optical microscopic imaging, mechanical design, synchronous control of photoelectric elements, optical shaping technology, etc.

Hongjin Li received her BS degree from Nanjing University in 2014 and her ME degree from Shanghai Institute of Optics and Fine Mechanics, CAS, in 2017. Currently, she is a PhD student in the Department of Biomedical Engineering at CityU, Hong Kong Centre for Cerebro-Cardiovascular Health Engineering, and Multiscale Precision Instrumentation Laboratory, CUHK. Her research interest includes advanced optical microscopic techniques.

Suyi Zhong received her BE degree from Central South University in 2018 and her ME degree from Tsinghua University in 2021. Currently, she is a PhD student at the College of Future Technology, Peking University, Beijing, China. Her research interests include light-sheet microscopy and lensfree microscopy.

Xinzhu Xu received his BS degree from Northwestern Polytechnical University in 2018. Currently, he is a joint PhD program student in the Department of Biomedical Engineering, Peking University, Georgia Institute of Technology and Emory University. His research interests include PSF modulation in microscopy, optoelectrical component control in microscopy, MINFLUX, STED, and SIM.

Fei Su received her master's of medicine (MM) degree from West China Clinical Medical College, Sichuan University in 2018. Currently, she is a PhD student at the Institute for Biomedical Materials and Devices (IBMD), Faculty of Science University of Technology Sydney, Australia, and a visiting scholar in the Department of Biomedical Engineering, Southern University of Science and Technology. Her research interests include bioimaging, pathological diagnosis and techniques, time-resolved pathological detection technology, artificial intelligence diagnostic system, biochemistry, and molecular biology.

Xi Peng received his BS degree from Shanxi University in 1998 and his PhD from Shanghai Institute of Optics and Fine Mechanics, Chinese Academy of Sciences, in 2003. Currently, he is a professor at the College of Future Technology, Peking University, Beijing, China. He is the author

of more than 80 journal papers and has written three book chapters. His current research interests include multimodality high-speed super-resolution fluorescence microscopy, lensfree microscopy, and two-photon STED hybrid microscope.

Dayong Jin received his PhD from Macquarie University of Australia in 2007. Currently, he is a fellow of the Australian Academy of Technology and Engineering, and is the head of the Joint Research Centre for Biomedical Materials and Instruments, University of Technology, Sydney, and Southern University of Technology, China. He has published more than 230 academic papers. His current research interests include bio-engineering optics, nanoprobe technology, biomedical diagnostics, precision optical instruments, and automation.

Karl Zhanghao received his BS degree from Peking University in 2012 and his PhD from Peking University and Georgia Institute of Technology. He is a research assistant professor in the Department of Biomedical Engineering, Southern University of Science and Technology. His research interests include super-resolution microscopy, multidimensional live-cell imaging, and fluorescence polarization microscopy.